Volume 9
Number 45
7 December 2021
Pages 25223–25674

Journal of Materials Chemistry A

Materials for energy and sustainability

rsc.li/materials-a

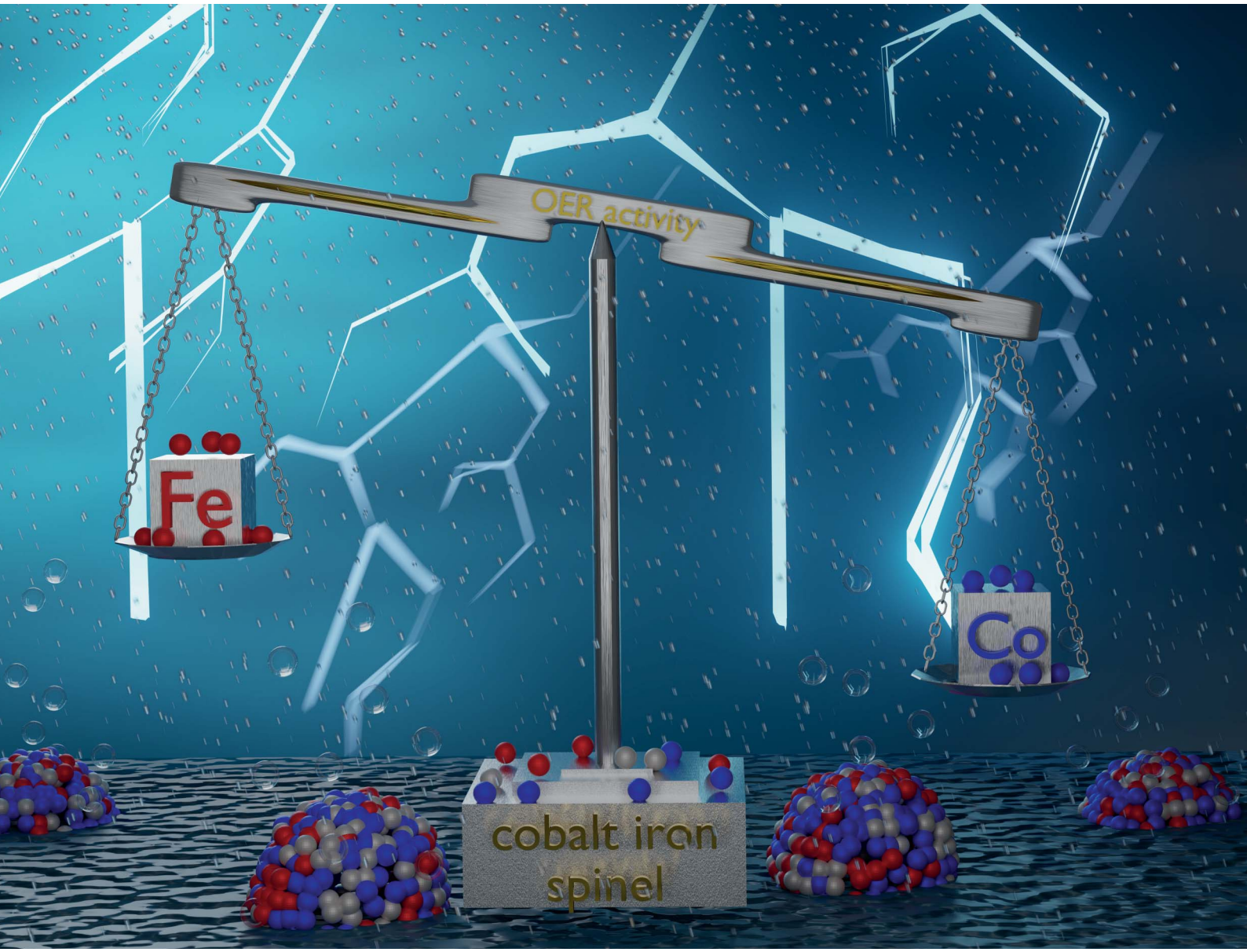

ISSN 2050-7488

ROYAL SOCIETY OF CHEMISTRY

PAPER
Stephan Schulz *et al.*
Influence of the cobalt content in cobalt iron oxides on the electrocatalytic OER activity

Journal of Materials Chemistry A

ROYAL SOCIETY OF CHEMISTRY

PAPER

View Article Online
View Journal | View Issue

Cite this: J. Mater. Chem. A, 2021, 9, 25381

Influence of the cobalt content in cobalt iron oxides on the electrocatalytic OER activity†

Sascha Saddeler,[a] Georg Bendt,[a] Soma Salamon,[b] Felix T. Haase,[c] Joachim Landers,[b] Janis Timoshenko,[c] Clara Rettenmaier,[c] Hyo Sang Jeon,[c] Arno Bergmann,[c] Heiko Wende,[b] Beatriz Roldan Cuenya[c] and Stephan Schulz *[a]

Received 3rd August 2021
Accepted 15th October 2021

DOI: 10.1039/d1ta06568h

rsc.li/materials-a

Sub 10 nm cobalt ferrite $Co_xFe_{3-x}O_4$ ($x \leq 1.75$) nanoparticles and cobalt-rich wüstite $(Co_{x/3}Fe_{(1-x)/3})O$ nanoparticles ($x \geq 2$) were synthesized in a solvothermal approach and characterized by powder X-ray diffraction (PXRD), selected area electron diffraction (SAED), transmission electron microscopy (TEM) as well as energy dispersive X-ray spectroscopy (EDX), IR, Raman, and ^{57}Fe-Mössbauer spectroscopy. Their electrocatalytic activity in the oxygen evolution reaction (OER) was evaluated and the active state formation was tracked by *operando* X-ray absorption spectroscopy (XAS). Our studies demonstrate that the cobalt-rich wüstite $(Co_{x/3}Fe_{(1-x)/3})O$ nanoparticles underwent a phase-transformation into the spinels $Co_xFe_{3-x}O_4$ ($x \geq 2$) under the applied OER conditions. The overpotential η_{10} at 10 mA cm^{-2}, serving as a benchmark for the OER activity of the cobalt ferrite nanoparticles in alkaline media, was lower than that of magnetite Fe_3O_4 even with low cobalt concentrations, reaching a minimum of 350 mV for $Co_{2.25}Fe_{0.75}O_4$ with a Tafel slope of 50 mV dec^{-1}. Finally, we identified that the catalytic activity is linked to the nanoparticle size as well as to the degree of Co redox activity and change in coordination during OER.

Introduction

The electrochemical water splitting reaction has been known for more than 200 years. This process offers easy access to the industrially important gases hydrogen and oxygen and is also becoming an important part of the modern energy economy.[1] In contrast to the hydrogen evolution reaction (HER), the four-electron-transfer oxygen evolution reaction (OER) is kinetically hindered on most electrode surfaces, resulting in high overpotentials (theoretical potential = 1.23 V). Cobalt seems to be an important ingredient for the synthesis of highly active electrocatalysts for the oxygen evolution reaction (OER) in alkaline media and a variety of cobalt materials, *i.e.* layered double hydroxides,[2,3] sulfides,[4] phosphides,[5,6] phosphates,[7] borides,[8,9] and spinel-type Co_3O_4,[10–12] showed promising catalytic activities with low overpotentials. Moreover, surface modification of Co-based electrocatalysts by introducing either metals or organic groups or placing them on porous carbon-based materials has been demonstrated to substantially increase their OER activity.[13–16] Unfortunately, the wide use of cobalt is not unproblematic due its toxic nature and the increasing global demand caused by the industrial production of batteries. The amount of cobalt in electrocatalysts should therefore be reduced as much as possible and replaced by non-toxic and earth abundant metals such as iron.[17]

Spinel-type mixed-metal oxides $A^{II}B_2^{III}O_4$ are particularly interesting as OER catalysts because the cationic sub-lattice is very tolerant to the substitution of other bivalent and trivalent cations, hence allowing a wide variation of the chemical composition and a fine-tuning of the catalytic properties. Moreover, they are very resistant to the harsh OER conditions as was recently shown for single $CoFe_2O_4$ nanoparticles with sub 5 nm size, which withstood OER conditions without changes in the morphology or crystal structure even at very high current densities in the range of several kA m^{-2}.[18,19] Spinel nanoparticles are accessible by a variety of synthetic routes, including hydrothermal,[20] co-precipitation,[21] sol–gel,[22] and solid-state approaches.[23] In solvothermal approaches, metal complexes are thermally decomposed in high-boiling solvents in the absence or presence of surfactants, so-called capping agents. This process not only allows the size- and morphology-controlled synthesis of spinel nanoparticles with precise control of the particle size down to 2–3 nm with narrow size distributions, but also gives access to

[a]Institute for Inorganic Chemistry, Center for Nanointegration Duisburg-Essen (CENIDE), University of Duisburg-Essen, Universitätsstr. 5-7, D-45117 Essen, Germany. E-mail: stephan.schulz@uni-due.de

[b]Faculty of Physics and Center for Nanointegration Duisburg-Essen (CENIDE), University of Duisburg-Essen, Lotharstr. 1, D-47057 Duisburg, Germany

[c]Department of Interface Science, Fritz-Haber Institute of the Max Planck Society, Faradayweg 4-6, 14195 Berlin, Germany

† Electronic supplementary information (ESI) available: Additional analytical data including PXRD, TEM, Mössbauer, XANES, EXAFS, magnetization curves. See DOI: 10.1039/d1ta06568h

hydrophobic[24,25] and hydrophilic nanoparticles depending on the solvent and surfactant.[26,27]

Metal acetylacetonates $M(acac)_x$ are commercially available precursors for the synthesis of spinel-type nanoparticles with various compositions, including monometallic M_3O_4 (M = Fe,[28] Co,[29] Mn[30]), heterobimetallic MFe_2O_4 (M = Mg, Mn, Co, Ni, Cu, Zn)[31,32] and even multimetallic materials such as $Mn_{0.5}Zn_{0.5}Fe_2O_4$.[33] Moreover, thermal decomposition of various amounts of such precursors allowed for the synthesis of material series with systematically varied compositions as was demonstrated for the synthesis of a series of $Co_xFe_{3-x}O_4$ nanoparticles, with x ranging from 0.5 to 2.[34] This is important since the degree of inversion in cobalt ferrite spinels $Co_xFe_{3-x}O_4$ is known to increase with the iron content.[35] We recently reported on the OER activity of ternary spinels $Co_xNi_{1-x}Fe_2O_4$ ($0 \leq x \leq 1$)[36] and $CoV_{2-x}Fe_xO_4$ nanoparticles ($0 \leq x \leq 2$),[37] which showed much lower overpotentials and Tafel slopes compared to the binary spinels $NiFe_2O_4$ and $CoFe_2O_4$, respectively. Apart from the chemical composition, the electrocatalytic activity of spinel nanoparticles also largely depends on their size and surface termination. Spherical, cubic, and octahedral $CoFe_2O_4$ nanoparticles as well as hexagonal plates and nanofibers were synthesized,[38–44] while we recently reported on the influence of the morphology and crystallographic surface termination on the electrocatalytic properties of Co_3O_4 nanoparticles.[45]

We herein became interested to investigate the influence of the cobalt content in spherical cobalt ferrite $Co_xFe_{3-x}O_4$ nanoparticles on their electrocatalytic activity. Our attempted solvothermal synthesis of a series of cobalt ferrite $Co_xFe_{3-x}O_4$ nanoparticles over the complete compositional range (x = 0–3, Δx = 0.25) yielded spherical spinel-type $Co_xFe_{3-x}O_4$ nanoparticles with cobalt contents below x = 2, whereas higher amounts of the Co precursor ($x \geq 2$) yielded biphasic mixtures of cobalt ferrite ($Co_xFe_{3-x}O_4$) and cobalt–iron wüstite ($Co_{x/3}Fe_{(1-x)/3}$)O nanoparticles. The size of the nanoparticles was found to depend on the Co content and decreased from 9 nm (x = 0) to 3 nm (x = 2.5). In addition, the activity of the cobalt ferrite as well as cobalt–iron wüstite nanoparticles in the OER in alkaline media is reported.

Results and discussion

I Nanoparticle synthesis and pre-catalyst characterization

Thermal decomposition of varying amounts of $Fe(acac)_3$ and $Co(acac)_2$ in triethylene glycol (TEG) in the presence of polyethyleneimine (PEI) as capping agent at 250 °C yielded sub 10 nm nanoparticles. The elemental composition of the nanoparticles was determined by EDX analyses (Table S1†), both of single nanoparticles and larger nanoparticle aggregates, proving that the initial Co : Fe precursor concentration is preserved in the resulting nanoparticles.

Even though the XRD diffractograms show broad Bragg reflections due the nanosized nature of the oxide phases (Fig. 1), the crystalline materials were identified as phase-pure cubic spinels $Co_xFe_{3-x}O_4$ in the case of cobalt contents $x \leq 1.75$ on the basis of the Bragg peak positions (2θ values of 30.2, 35.6, 43.4, 57.2 and 62.6°), which correspond to the (220), (311), (400), (511), and (440) lattice planes (Fe_3O_4, PDF 01-077-1545, with a = 8.3970 Å). In contrast, higher concentrations of the cobalt precursor (x = 2.00–2.75) yielded biphasic mixtures of cobalt ferrite ($Co_xFe_{3-x}O_4$) and cobalt–iron wüstite ($Co_{x/3}Fe_{(1-x)/3}$)O, resulting in a shoulder within the broad reflex at 43°. The fraction of the rock-salt phase as quantified by Rietveld refinement (Fig. S1 and Table S1†) was found to increase with increasing Co precursor concentration (x = 2.00, 30%; x = 2.25, 57%; x = 2.50, 90%; x = 2.75, 99%). The rock salt cobalt–iron wüstite phase was identified by Bragg reflections at 2θ = 36.5 and 34.4°, corresponding to the (111) and (200) lattice planes of this structure (CoO, PDF 01-071-1178, with a = 4.2631 Å). The Co-richest material within this series, iron-free cobalt(II) oxide CoO, formed a biphasic mixture of rock salt and wurtzite-type phases (CoO, PDF 01-089-2803). The phase transition from the cobalt ferrite ($Co_xFe_{3-x}O_4$) to the cobalt–iron wüstite ($Co_{x/3}Fe_{(1-x)/3}$)O phase is also described in the Co–Fe–O phase diagram for cobalt-rich samples for low oxygen partial pressures.[46]

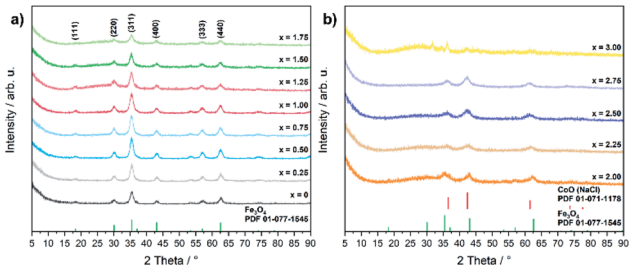

Fig. 1 PXRD patterns of (a) $Co_xFe_{3-x}O_4$ (x = 0–1.75) and (b) $Co_xFe_{3-x}O_4/(Co_{x/3}Fe_{(1-x)/3})O$ (x = 2–3) with references for Fe_3O_4 (PDF 01-077-1545) and CoO (PDF 01-071-1178).

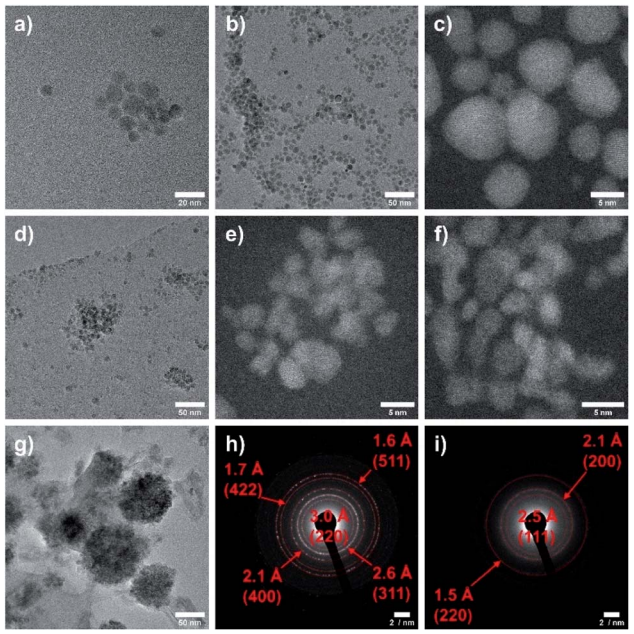

Fig. 2 TEM images of $Co_xFe_{3-x}O_4$ for x = 0 (a), 0.50 (b), 1.00 (c), 1.50 (d), 2.00 (e), 2.50 (f) and 3.00 (g) as well as SAED images for x = 1.00 (h) and 2.50 (i).

Fig. 2 shows TEM images of $Co_xFe_{3-x}O_4$ nanoparticles, proving the spherical morphology for all nanoparticles. The average particle size as-determined by analyzing 100 particles was found to decrease with increasing Co content from 9 nm ($x = 0$) to 3 nm ($x = 2.50$) (Fig. S2†) as was previously observed by Jalili and coworkers.[47]

The steadily decreasing size of the nanoparticles with increasing Co content was only observed for particles synthesized with PEI as surfactant, whereas analogous nanoparticles prepared in the absence of PEI showed constant particle sizes of 5–6 nm independent of the Co content, indicating that PEI differently binds to iron and cobalt. The binding strength of ligands to both the molecular metal precursor and the resulting nanoparticle surface is generally known to largely affect the nucleation and growth rates and consequently the final nanoparticle size.[48] The low magnification micrograph shows well separated nanoparticles with a low tendency for agglomeration and a narrow size distribution except for the iron-free material (Fig. 2g). The average size of the $CoFe_2O_4$ nanoparticles is 8 nm, and the DF-STEM image (Fig. 2c) shows crystalline nanoparticles with a *d*-spacing of 2.53 Å corresponding to the (311)-lattice plane of $CoFe_2O_4$. In contrast, the DF-STEM image of biphasic nanoparticles ($x = 2.50$) (Fig. 2f) shows lattice fringes with a *d*-spacing of 2.46 Å, corresponding to the (111)-plane of the cubic CoO phase. The assignment of the crystalline phases $CoFe_2O_4$ and CoO is supported by the respective selected area electron diffraction (SAED) patterns (Fig. 2h and i).

The core-level XPS spectrum (Fig. S3†) for the Co 2p region shows the characteristic $2p_{3/2}$ and $2p_{1/2}$ peaks at *ca.* 779 and 795 eV, respectively. A satellite peak is visible for both peaks at higher binding energies of *ca.* 785 and 802 eV. These satellites are the signature for octahedrally coordinated high-spin Co^{2+} ions. Neither octahedrally coordinated low-spin Co^{3+} nor tetrahedrally coordinated Co^{2+} ions exhibits this feature. A high amount of Co^{2+} ions can be identified for $x = 0.50$ *via* peak shift to *ca.* 781 eV. Furthermore, the intensity of the satellite peak at *ca.* 785 eV decreases for higher amounts of Co from $x = 1.00$ to 1.50, indicating the presence of Co^{3+} ions.[49,50] The octahedrally-coordinated CoO_6 unit was found for sample $x = 1.50$ at *ca.* 779 eV, whereas the tetrahedrally-coordinated CoO_4 unit is visible at *ca.* 781 eV.[51] In contrast, the biphasic materials ($x = 2.25$, 2.50) show more pronounced satellites due to the presence of high amounts of Co^{2+}, in accordance with the formation of the rock salt phase $(Co_xFe_{1-x})O$, which exclusively contains bivalent Co. Cobalt-poor samples ($x = 0.50$, 1.00, 1.50) show peaks at *ca.* 711 and 724 eV in the Fe 2p region, which can be attributed to the Fe $2p_{3/2}$ and Fe $2p_{1/2}$ of Fe_3O_4.[52] The satellite peak at 717 eV, which is characteristic for the presence of Fe^{2+} ions,[53] increases with higher cobalt contents until only a weak satellite is visible in the sample with $x = 1.75$.

The nanoparticles were also characterized by FTIR and Raman spectroscopy. The spinel-type structure consists of tetrahedral MO_4 and octahedral MO_6 units (M = Co, Fe), which show characteristic signatures in the FTIR and Raman spectra. The spinel-type structure has five Raman active phonon modes (A_{1g}, E_g, three T_{2g}), while the A_{1g} mode in inverse spinels such as $CoFe_2O_4$ splits into two modes, A_{1g} and A_{1g*}. Only two of them, A_{1g} and T_{2g}, are visible as broad modes in the Raman spectrum shown in Fig. S3a.† The A_{1g} mode around 700 cm^{-1} most likely originates from the symmetric stretching of the MO_4 tetrahedra and the T_{2g} mode originates from the MO_6 octahedra, even though this assignment is controversially discussed in the literature.[54] According to Laguna-Bercero *et al.*[55] the AO_4 unit cannot be differentiated from the BO_6 unit due to weaker A–O bonds compared to B–O bonds, which results in a mixture of both vibrations within the A_{1g} mode. Both modes shift to lower wavenumbers with increasing cobalt content up to $x = 1.75$ due the incorporation of cobalt into the spinel-type structure as was previously reported.[56] Starting at $x = 2.0$, the two bands not only shift back to higher wavenumbers but also become sharper with increasing value of x, and the E_g mode also becomes visible for $x = 2.75$ and $x = 3.0$, respectively. In contrast to the XRD results, only the spinel-type and not the wüstite-type phase was detected for high cobalt contents up to $x = 3$, most likely due to the ease with which CoO can be oxidized to Co_3O_4 even at moderate laser power.[54] The influence of laser power on the transformation is shown in Fig. S3b,† and biphasic samples ($x = 2$–3) were measured at low laser power.

Cobalt ferrite not only shows five Raman active modes but also four IR-active modes (4 F_{1u}). The FTIR spectra (Fig. S4†) show two major absorption bands at 386 and 579 cm^{-1} for the

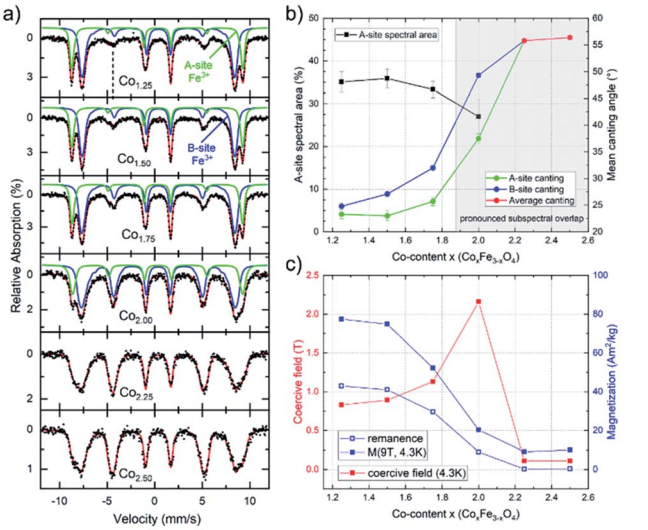

Fig. 3 (a) In-field Mössbauer spectra of $Co_xFe_{3-x}O_4$ ($x = 1.25$–2.5) nanoparticles, illustrating contributions of A- (green) and B-site (blue) subspectra. Spin canting angles were determined from the relative intensities of line 2 (marked by dashed line) and 5, strongly increasing upon rising Co-content. (b) Parameters extracted from in-field Mössbauer spectroscopy of $Co_xFe_{3-x}O_4$ ($x = 1.25$–2.5) nanoparticles: The determination of the A-site spectral area (black) is hindered at $x > 1.75$ (shaded area) due to pronounced A- and B-subspectral overlap, spin canting angles of A- (green) and B-sites (blue) are provided up to $x = 2.0$. For higher Co-content the antiferromagnetic behavior prevents the resolution of the Fe-contributions on tetrahedral and octahedral positions and therefore, the average spin canting angles (red) are shown. (c) Remanent magnetization $M_{(4.3\ K,0\ T)}$ (blue, empty), high-field magnetization $M_{(4.3\ K,9\ T)}$ (blue, full) and coercive fields (red) determined at 4.3 K.

$CoFe_2O_4$ nanoparticles corresponding to the characteristic vibrations of octahedral MO_6 (M = Co, Fe) unit and the tetrahedral MO_4 unit, respectively.[57] Both bands shift slightly, most likely due to a changing degree of inversion, but no clear trend is visible. Weak absorption bands around 1600, 1450, 1115 and 1059 cm^{-1} indicate the presence of small amounts of the organic capping agent (TEG, PEI) bonded to the nanoparticle surface.[58,59]

To further probe the composition-dependent structural properties using the underlying magnetic characteristics, Co_x-$Fe_{3-x}O_y$ nanoparticles with Co-contents of $x = 1.25$–2.50 were characterized *via* Mössbauer spectroscopy as well as magnetometry (Fig. 3).

Mössbauer spectra were recorded at 4.3 K in an applied field of 5 T (parallel to the γ-ray propagation direction) to determine the distribution of Fe^{3+} ions across different crystallographic sites, also allowing us to thereby (indirectly) extract the Co-ion site occupation. As shown in Fig. 3, samples with lower Co-content ($x = 1.25$–1.75) show a typical spinel spectrum with a clear separation between the sextet subspectra of the tetrahedrally coordinated A-sites (green) and octahedrally coordinated B-sites (blue). From the ratio of the spectral areas of these two sites, the degree of inversion can be calculated. As our samples deviate from the standard stoichiometry given above (AB_2O_4), a representation of the ion distribution *via* the inversion parameter would be uncommon. Thus, we present the ion site occupation by plotting the relative spectral area of Fe-ions on the A-site in Fig. 3a, which allows us to draw conclusions on the changing site preference upon increasing x. The displayed relative A-site spectral areas range from 33(1) % to 36(2) % for $1.25 \leq x \leq 1.75$, which is slightly below the inversion parameter values commonly reported for pure bulk cobalt ferrite.[60] Nonetheless, a more random placement is not unusual for nanoparticulate spinel systems, depending on the utilized synthesis procedure.

The finding from in-field Mössbauer spectroscopy regarding a rather random site-occupation is substantiated by the high magnetization values $M_{(4.3\ K,9\ T)}$ (Fig. 3c) and also illustrated in detail in the ESI.† The spectra with low Co-content are also characteristic in terms of revealing only a moderate degree of spin canting, which is shown by the intensities of lines 2 and 5 relative to lines 3 and 4, respectively. This indicates that the magnetic moments are predominantly aligned in the external field, with the small residual spin canting angle, as also given in Fig. 3b, presumably stemming from spin frustration effects at the surface. Upon increasing the Co-content ($x \geq 2.0$) in these samples, two main effects can be observed. On the one hand, the average spin canting angles for both sites increase, as is visible by the increasing intensity of lines 2 and 5 in Fig. 3a. On the other hand, the two sextet subspectra increasingly overlap, making it impossible to accurately determine the contribution of the individual sites. Therefore, spectra were reproduced with only one distribution of effective magnetic fields for $x > 2.0$, where we observe a completely random orientation of the probed spins, as indicated by reaching the "magic angle" ($\approx 54.7°$). Such a behavior points towards a transition of the material from a ferrimagnetic state of the CFO endmember towards an increasingly antiferromagnetic state, as is typical for Co_3O_4, while the decreasing average particle diameter upon rising x will also likely result in stronger surface spin canting. Although X-ray diffractograms show the formation of a CoO phase for compositions with $x > 2$ (Fig. 1b), the comparatively high hyperfine fields and the isomer shifts of *ca.* 0.48 mm s^{-1} in the Mössbauer spectra point towards Fe^{3+} rather than the Fe^{2+} species one would expect for a Fe-fraction present within a wüstite-like CoO phase. For compositions up to $x = 2.50$, this can be resolved assuming a nearly Fe-free CoO main phase, while the increasingly minor Co_3O_4 phase (Table S2†) contains sufficient residual amounts of Fe, thus being much more strongly present in the Mössbauer spectra. As the CoO main phase is also antiferromagnetic,[61] the low magnetization in the $M(H)$ loops (Fig. S6b†) is consistent with this interpretation, as is the generally antiferromagnetic nature of the Mössbauer spectra for $x > 2$, preventing the resolution of individual subspectra due to a lack of orientation of magnetic moments relative to the applied magnetic field (Fig. 3a).

II OER activity

The electrochemical OER activity of as-prepared cobalt ferrite $Co_xFe_{3-x}O_4$ ($x = 0$–1.75) and cobalt–iron wüstite $(Co_{x/3}Fe_{(1-x)/3})O$ ($x \geq 2$) nanoparticles was determined using a rotating disk electrode. The nanoparticles were embedded in Nafion® on glassy carbon working electrodes in a standard three-electrode system with 1 M iron-free KOH as electrolyte and a Pt counter electrode at room temperature. To test the influence of solution of Pt ions from the counter electrode a linear sweep was performed with a graphite counter electrode (Fig. S8†). A catalyst loading of 100 μg cm^{-2} based on the geometrical surface area (0.196 cm^2) was used for all experiments. Additionally, the OER activity and stability of $CoFe_2O_4$ ($x = 1$) was tested for catalyst loadings of 50 and 200 μg cm^{-2} (Fig. S9†). The working electrodes were activated by cyclic voltammetry (CV) with a scan rate of 100 mV s^{-1} in a potential window between 1 and 2 V *vs.* RHE until reproducible voltammograms were obtained and linear sweep voltammogram (LSV) measurements with a scan rate of 5 mV s^{-1} were recorded afterwards (1–2 V *vs.* RHE). The benchmark for evaluating electrocatalysts is the overpotential η_{10}, which is necessary to deliver a geometric current density of 10 mA cm^{-2}.[62]

Fig. 4a and b display the polarization curves for the Co_x-$Fe_{3-x}O_4$ ($x = 0$–1.75) and $(Co_{x/3}Fe_{(1-x)/3})O$ ($x \geq 2$) nanoparticles. The cobalt-free Fe_3O_4 nanoparticles show only a very low electrocatalytic activity and the highest overpotential (699 mV) within this material series. The introduction of a small fraction of cobalt ($x = 0.25$) leads to a significant reduction of the overpotential by 250 mV, reaching a value that is comparable to the overpotential of Co_3O_4 ($\eta = 440$ mV).[63] The overpotential further decreases monotonically with increasing cobalt content and reaches a minimum at $\eta_{10} = 350$ mV for the composition $Co_{2.25}Fe_{0.75}O_4$. Increasing cobalt content ($x > 2.25$) then leads to an increase of the overpotential, which reaches a maximum for the pure cobalt oxide (CoO) at $\eta_{10} = 410$ mV.

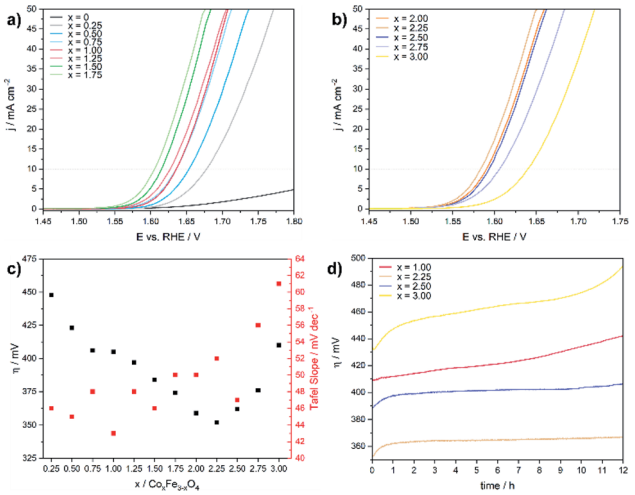

Fig. 4 Linear sweep voltammograms for (a) $Co_xFe_{3-x}O_4$ ($x = 0$–1.75) and (b) $(Co_{x/3}Fe_{(1-x)/3})O$ ($x \geq 2$) in 1 M KOH electrolyte with a scan rate of 5 mV s^{-1}, (c) overpotential and Tafel slope *versus* the cobalt content and (d) chronoamperometry measurements at 10 mA cm^{-2} (geometrical surface area).

Fig. 4c shows the Tafel slopes for the $Co_xFe_{3-x}O_4$ ($x = 0$–2) and $(Co_{x/3}Fe_{(1-x)/3})O$ ($x \geq 2$) nanoparticles, and Fig. S10† shows the overpotential η is plotted against the logarithmic current density log (j). All electrocatalysts show Tafel slopes in a narrow range of 43–61 mV dec^{-1}. A low Tafel slope indicates favourable OER reaction kinetics which can imply differences in the OER surface chemistry.[64,65] The observed trend for the Tafel slope is comparable with the trend visible for a series of $CoV_{2-x}Fe_xO_4$ ($0 \leq x \leq 2$)[37] and $Co_{1-x}Ni_xFe_2O_4$ ($0 \leq x \leq 1$)[36] nanoparticles. Fig. 4d displays chronoamperometry measurements at 10 mA cm^{-2} for $CoFe_2O_4$ ($x = 1$), which were performed to investigate the stability of the nanoparticles under these conditions. The increasing overpotential with increasing measurement time can be caused by several processes like nanoparticle growth, detachment, dissolution and compositional changes. For instance, leaching of Co^{2+} ions from the nanoparticle surface into the solution as was previously reported[66] would result in cobalt vacancies or Fe accumulation on the nanoparticle surface and reduce the number of cobalt atoms on the surface. The reduced cobalt content should lead to a decrease of the OER activity as we observed in the LSV curves for spinel compounds with low amounts of cobalt. In contrast, the phase mixtures of spinel and rock salt type materials ($x = 2.25$, 2.50) show a constant overpotential over time. The observed rising overpotential for the CoO nanoparticles ($x = 3.00$) can be attributed to the oxidation of Co^{2+} to Co^{3+} under electrochemical conditions over the formation of $Co(OH)_2$, CoO(OH) and finally Co_3O_4.[67–69] The long-term stability in OER was also investigated by chronoamperometric measurement of $CoFe_2O_4$ ($x = 1$) at 1 mA cm^{-2} over 48 h (Fig. S11†) with a slight increase of the potential most likely due to leaching of Co into solution.

Electrochemical impedance spectra (EIS) were recorded to gain further insights in the electron transfer kinetics. Fig. 5 shows the Nyquist plots for the $Co_xFe_{3-x}O_y$ nanoparticles at an overpotential of 550 mV.

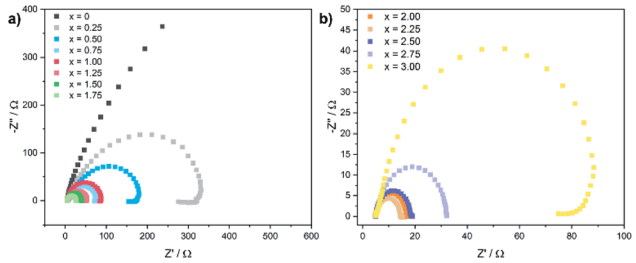

Fig. 5 Electrochemical impedance spectra (EIS) for (a) $Co_xFe_{3-x}O_4$ ($x = 0$–1.75) and (b) $(Co_{x/3}Fe_{(1-x)/3})O$ ($x \geq 2$) nanoparticles recorded at an overpotential of 550 mV.

With increasing cobalt content, the semicircular arc becomes narrower up to $x = 2.25$ and widens up again with further increase of x. The charge-transfer resistance R_{ct} was extracted by fitting the Nyquist plot using a Randles circuit. The cobalt-free catalyst exhibits very high values for R_{ct} with ~2000 Ω (Fe_3O_4). Similarly to the behaviour of the overpotential and the Tafel slope, R_{ct} also decreases rapidly with increasing cobalt content and reaches a minimum value of 10 Ω for $x = 2.25$, increasing slightly up to 90 Ω for $x = 3.00$. The substitution of iron by cobalt in the cationic sublattice of the spinel structure obviously leads to a significantly improved charge transport for nanoparticles with a cobalt-rich composition, which is in good agreement with the observed dependence of the Tafel slope and the overpotential on the elemental composition.

III *Operando* characterization

Operando X-ray absorption spectroscopy (XAS) measurements were conducted at the Co and Fe K-edges for four different nanoparticle compositions: $Co_{2.25}Fe_{0.75}O_4$, $CoFe_2O_4$, $Co_{0.25}Fe_{2.75}O_4$ and CoO_X. Thus, the metal ion chemical state and local atomic structure could be determined for the most important cases of the composition–activity profile. The *operando* XAS data of the catalysts were recorded in the as-prepared state, after an electrochemical conditioning treatment (20 CVs, 1–1.8 V_{RHE}, 50 mV s^{-1}) in the OER active state at +1.8 V_{RHE} as well as after OER in the electrolyte at +1.0 V_{RHE}. All measurements were carried out in 0.1 M KOH. All spectra are provided in the ESI (Fig. S7–S13†) including a table with all fitting parameters (Table S6†).

The X-ray absorption near edge structure (XANES) spectra of $Co_{2.25}Fe_{0.75}O_4$, $CoFe_2O_4$, $Co_{0.25}Fe_{2.75}O_4$ and CoO_X at the Co K- and Fe K-edge are provided in Fig. 6a and b and S12a–e.† The corresponding oxidation states of Co and Fe were calculated by comparison of the absorption edge position with known reference compounds.[70–72] The extracted oxidation states are displayed in Fig. 6c for Co and Fig. S12f† for Fe, with an uncertainty of ±0.1 and ±0.2 for Co and Fe, respectively. The average Co oxidation state increases for all samples during OER and this oxidation process is partially reversible as the Co oxidation state after OER exhibits a reduction. The average oxidation state of Fe is close to +3 for all samples and changes significantly less than

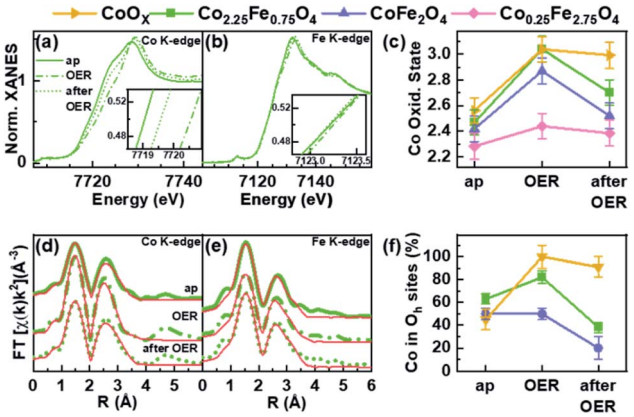

Fig. 6 (a) Co and (b) Fe K-edge XANES of $Co_{2.25}Fe_{0.75}O_4$ nanoparticles as-prepared (ap), during OER at 1.8 V_{RHE} and after OER at OCV at ~1 V_{RHE}. (c) Co oxidation state ap, during and after OER of $Co_{2.25}Fe_{0.75}O_4$, $CoFe_2O_4$, $Co_{0.25}Fe_{2.75}O_4$ and CoO_X nanoparticles. (d) Co and (e) Fe K-edge EXAFS of $Co_{2.25}Fe_{0.75}O_4$ nanoparticles and (f) the fraction of Co ions occupying available octahedral sites.

that of Co under the different electrochemical conditions, especially considering the error bars. In detail, we identified that the average initial Co oxidation state ranges from +2.3 to +2.6, which increases with the percentage of Co within the sample. The initial Fe oxidation state as-prepared is +2.8 to +3, with no distinct trend with nanoparticle composition. During OER, the Co oxidation state increases from +2.4 to +3.0. The cobalt-rich CoO_X and $Co_{2.25}Fe_{0.75}O_4$ exhibit the highest Co oxidation state of +3.0, followed by $CoFe_2O_4$ with +2.9 and $Co_{0.25}Fe_{2.75}O_4$ with +2.4. All samples possess an Fe oxidation state ranging from +2.9 to +3.0 during OER. After OER, the cobalt oxidation decreases to +2.5 and +2.7 for $CoFe_2O_4$ and $Co_{2.25}Fe_{0.75}O_4$, respectively, but stays constant within error bars for CoO_X and $Co_{0.25}Fe_{2.75}O_4$. In this regard, the $Co_{2.25}Fe_{0.75}O_4$ and $CoFe_2O_4$ nanoparticles reduce stronger after OER than the $Co_{0.25}Fe_{2.75}O_4$ and CoO_X nanoparticles, implying a larger redox activity of the Co ions. The Fe oxidation state after OER remains unchanged within the error. Interestingly, the so-called white line position (energy of the intensity maximum) of the Fe XANES profile for $Co_{2.25}Fe_{0.75}O_4$ shifts reversibly from 7131.5 eV to 7132.5 eV, which indicates subtle changes in the electronic structure under OER conditions.

The extended X-ray absorption fine structure (EXAFS) analysis for bimetallic $Co_XFe_{2-X}O_4$ nanoparticles was carried out based on a spinel-structure with a fixed 2 : 1 ratio of octahedral and tetrahedral site occupancy (see ESI† for further details). This analysis was carried out at both the Co and Fe K-edges for $Co_{2.25}Fe_{0.75}O_4$ and $CoFe_2O_4$ nanoparticles. The $Co_{0.25}Fe_{2.75}O_4$ nanoparticles were excluded from the former analysis due to insufficient data quality caused by the low Co content. For the CoO_x nanoparticles, the same model was applied without a fixed 2 : 1 ratio to determine the fraction of octahedrally-coordinated Co ions in the presence of the wurtzite-CoO phase. The fits are displayed in Fig. 6d, e and S11a–e† for measurements carried out on the as-prepared samples, during OER and after OER. The first peak corresponds to the M–O coordination at ~1.6 Å (phase uncorrected). The peak of the second coordination shell at 2.5 Å (phase uncorrected) corresponds to two di-μ-oxo bridged metal ions in octahedral sites. A third coordination shell peak at 3.1 Å (phase uncorrected) originates from mono-μ-oxo bridges between metal ions occupying tetrahedral and octahedral sites.[73,74]

As discussed above, the wüstite CoO_X nanoparticles do not exhibit a spinel structure and the XANES can be best described as a linear combination of rs-CoO, w-CoO and CoOOH reference spectra. In the as-prepared state, the EXAFS spectra show a pronounced contribution of the second coordination shell due to the occupation of octahedral sites, and some contribution in the third coordination shell from tetrahedral sites as-prepared. During OER, a CoOOH-like structure with only octahedral sites occupied is formed, which is typical for cobalt oxides. After OER, the pure CoO_x nanoparticles were found to restructure, as some tetrahedral sites are occupied with Co ions afterwards leading to a Co_3O_4-like structure.

Fig. 6f shows the fraction of Co located in available octahedrally coordinated sites in CoO_X, $Co_{2.25}Fe_{0.75}O_4$ and $CoFe_2O_4$ nanoparticles. As-prepared, the fraction is highest for $Co_{2.25}Fe_{0,75}O_4$ and similar for CoO_X and $CoFe_2O_4$. During OER, the fraction of Co occupying the octahedral sites is larger than before and/or after OER and thus, linked to the oxidative reaction conditions and an (irreversible) increase in the average Co oxidation state. This process is strongest yet irreversible for CoO_X and lowest for $CoFe_2O_4$. It is not surprising that CoO_X forms a CoOOH-like structure under OER conditions with all Co octahedrally coordinated. Remarkably during OER, the most active $Co_{2.25}Fe_{0.75}O_4$ catalyst exhibits an increase in octahedral sites occupied by Co whereas the less-active $CoFe_2O_4$ is almost identically unchanged as compared to the state after OER. Recently, octahedral di-μ-oxo bridges have been identified as a common structure formed during OER independent of the initial crystal structure including Co_3O_4 spinel oxides.[65] After OER we notice a decrease of octahedrally coordinated Co which arises as tetrahedrally coordinated sites of the third coordination shell. The EXAFS fits furthermore revealed that the identified reversible oxidation of the Co ions results in a contraction of the average Co–O bond during OER by 0.03–0.04 Å for all analysed samples as compared to after OER. The di-μ-oxo bridges and mono-μ-oxo bridges contract by 0.01–0.02 Å for Co ions. The Fe–M distances contract within ~0.02 Å for second and third coordination shell.

In summary, XANES and EXAFS analyses suggest an increasing average Co oxidation state with increasing Co content in the as-prepared state. The most active $Co_{2.25}Fe_{0.75}O_4$ shows pronounced (reversible) changes in the Co oxidation state as well as di-μ-oxo bridges during OER, which is similar to pure CoO_X nanoparticles. This contrasts with $CoFe_2O_4$ nanoparticles which show a strong Co oxidation during OER but miss the transformation during OER. $Co_{0.25}Fe_{2.75}O_4$ nanoparticles do not show changes, underlining their low reactivity. In general, the Fe ions do not undergo a pronounced redox transition during OER and the Fe K-edge data do not show strong Fe oxidation or Fe–O contraction. It must be noted that based on the *operando* XAS results, the Co ions participate

significantly stronger in the redox chemistry and the degree of average structural change during OER, as referred to the post-catalysis state is linked to the catalytic activity.

IV Post-catalyst characterization

The OER is performed in strong alkaline media under high potentials and current densities which can lead to structural and chemical changes of the electrocatalyst. We therefore performed a post-catalysis characterization of the nanoparticles. EDX analyses of the bulk $CoFe_2O_4$ spinel nanoparticles show no change of their chemical composition after catalysis.

The crystalline structure of the spinel nanoparticles ($x < 2$) was unaffected by OER conditions according to XRD and SAED analyses. This agrees with the reversible structural transformation determined by *operando* XAS and previous reports.[14] However, the formation of very small nanoparticles (1–2 nm) was observed for $CoFe_2O_4$ ($x = 1$) (Fig. 7b), which could not be analyzed in more detail due to their small size. Additionally, the elemental composition becomes less homogeneous in a single particle after electrochemical treatment (Fig. 7c and d). However, these data should be regarded with care since only a single particle was analysed. In contrast, the cobalt–iron wüstite nanoparticles underwent major structural changes during OER and were transformed into the spinel-type structure as was proven by SAED ($x = 2.25$, 2.50, Fig. 7e and f) and GIXRD ($x = 2.50$, Fig. 8) with no residues of rock salt type material. The characteristic reflections due to the iron–cobalt wüstite phase disappeared, whereas reflections due to the spinel structure are present. These findings agree with the results obtained by *operando* XAS.

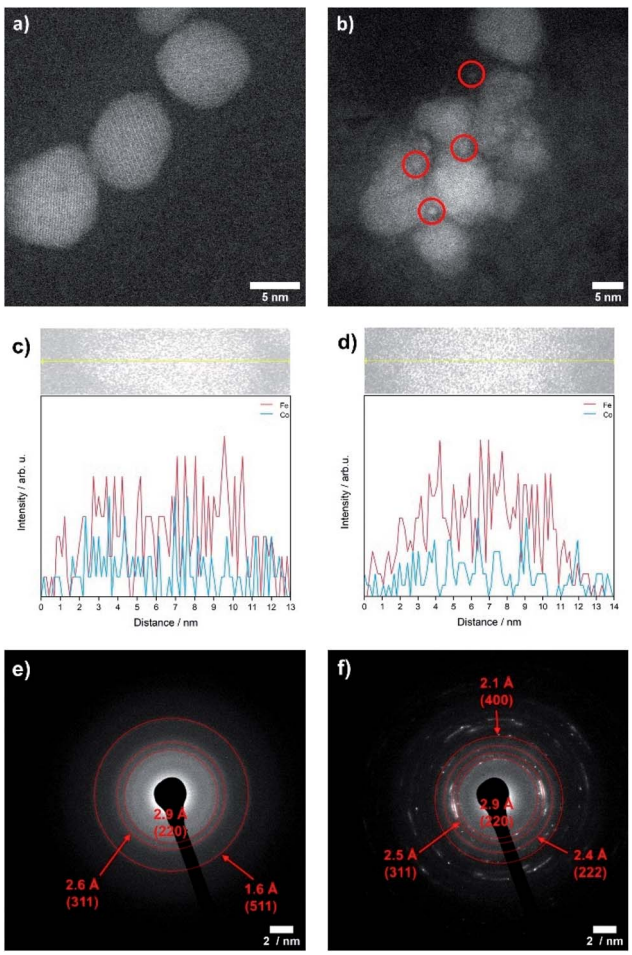

Fig. 7 TEM images of $CoFe_2O_4$ ($x = 1$) nanoparticles before (a) and after OER (b), TEM-EDX linescans on a single particle for $CoFe_2O_4$ ($x = 1$) before (c) and after electrochemical treatment (d) and SAED patterns after OER measurements for $Co_xFe_{3-x}O_4$ with $x = 2.25$ (e) and 2.50 (f).

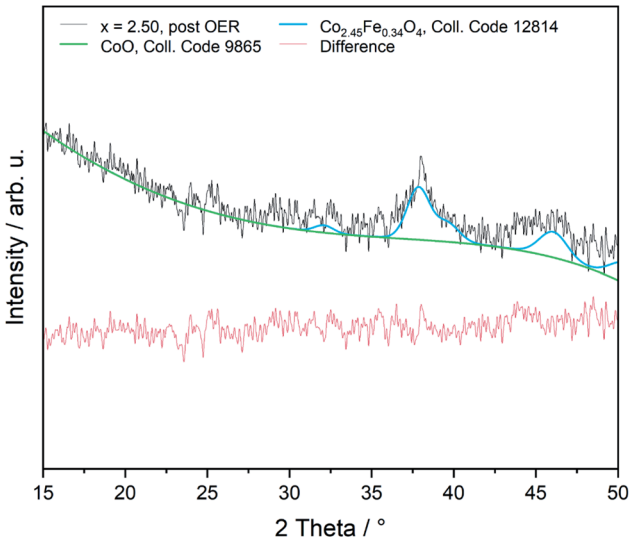

Fig. 8 Rietveld refinement of sample $x = 2.50$ on Si after OER measurement (GIXRD, 1°).

Conclusions

A series of sub 10 nm PEG/PEI stabilized phase-pure cobalt ferrite $Co_xFe_{3-x}O_4$ ($x \leq 1.75$) and cobalt-rich cobalt–iron wüstite $(Co_{x/3}Fe_{(1-x)/3})O$ nanoparticles ($x \geq 2$) were synthesized and characterized by EDX, XRD, TEM, IR and Raman spectroscopy. A rather random ion site-occupation with a minor Co B-site preference was found by in-field Mössbauer spectroscopy, in agreement with magnetometry results. The nanoparticles were tested as OER catalyst in alkaline media, and *operando* XAS measurements revealed a correlation of the content of di-μ-oxo bridged cobalt–metal sites and the extent of reversible Co oxidation state change during OER with the reactivity. Post catalysis GIXRD and SAED analyses revealed the phase transition of iron–cobalt wüstite $(Co_{x/3}Fe_{(1-x)/3})O$ ($x \geq 2$) nanoparticles into the spinel phase. The introduction of cobalt into the spinel structure improves the OER reaction kinetics and the charge transport of the nanoparticles, resulting in a reduction of the onset potential and the overpotential η_{10} for the OER compared to the cobalt-free Fe_3O_4. A maximum OER activity is reached for $x = 2.25$, whereas a further increase of the Co content results in a steady increase of the overpotential.

Experimental

Synthetic procedures

Materials. Cobalt(II)acetylacetonate $Co(acac)_2$ (99%), iron(III) acetylacetonate $Fe(acac)_3$ (97%), polyethylenimine (branched, $M_w = 800$ by LS) (PEI) and triethylene glycol (99%) (TEG) were purchased from Sigma-Aldrich and used without further purification.

Synthesis of cobalt ferrite $Co_xFe_{3-x}O_4$ ($x \leq 1.75$) and cobalt–iron wüstite ($Co_{x/3}Fe_{(1-x)/3}$)O nanoparticles ($x \geq 2$). 150 mg PEI as well as $Co(acac)_2$ and/or $Fe(acac)_3$ (Table S7†) were suspended in 10 g of TEG and stirred for 1 h at 120 °C in the open reaction vessel to remove volatile contaminations. The resulting clear solution was stirred at 250 °C for 1 h in a closed reactor vessel and then cooled to ambient temperature. Addition of a 1 : 1 mixture of acetone and ethyl acetate resulted in precipitation of the $Co_xFe_{3-x}O_y$ nanoparticles, which were isolated by centrifugation (3000 rpm, 10 min), washed two times with acetone and dried at ambient temperature.

Methods

Powder X-ray diffraction (PXRD). PXRD patterns of the nanoparticles were recorded at ambient temperature (25 ± 2 °C) using a Bruker D8 Advance powder diffractometer in Bragg–Brentano mode with Cu Kα radiation ($\lambda = 1.5418$ Å, 40 kV and 40 mA). The powder samples were investigated in the 2θ range of 5 to 90° with a step size of 0.01° (2θ) and a counting time of 0.3 s. The amount of catalyst, which is typically used for OER on the GC-electrode, is not sufficient for standard XRD measurements. Therefore, the OER measurement was repeated with 2 mg catalyst loaded on highly conductive Si(100) substrates. After OER, the loaded silicon substrates were used as sample holder for grazing incidence X-ray diffraction (GIXRD) measurements, which were recorded using a Panalytical Empyrean diffractometer with Cu-Kα radiation ($\lambda = 1.5418$ Å, 40 kV, 40 mA) and a fixed angle of incidence of 1°. The films were investigated in the 2θ range of 5 to 90° with a step size of 0.05° (2θ).

Transmission electron microscopy. The size and morphology of the nanoparticles were analyzed by using a JEOL 2010 (200 kV) transmission electron microscope. Energy-dispersive X-ray spectroscopy (EDS) studies were carried out on a scanning electron microscope (Jeol JSM 6510) equipped with an EDS device (Bruker Quantax 400), and the spectra were quantified using the software Esprit 1.9 (Bruker).

Infrared spectroscopy (IR). IR spectra were recorded with an ALPHA-T FT-IR spectrometer equipped with a single-reflection ATR sampling module.

Raman spectroscopy. Raman spectra were recorded with a Renishaw InVia-Raman spectroscope using a laser with a wavelength of 633 nm ($P_{max} = 15$ mW, mag. 50×) with 6 s exposure time and 30 repeats.

Magnetometry. Magnetic properties were investigated using the vibrating sample magnetometer (VSM) option of a Quantum Design PPMS DynaCool. Field-dependent magnetization was analyzed *via* $M(H)$ curves recorded at temperatures of 4.3 K and 300 K up maximum fields of ±9 T, while temperature-dependent magnetization $M(T)$ was characterized by recording zero field cooled – field cooled (ZFC–FC) curves with a sweep rate of 2 K min^{-1} between 5 K and 320 K under an applied magnetic field of 10 mT.

Mössbauer spectroscopy. Measurements on dry powder samples were performed in transmission geometry, using a $^{57}Co(Rh)$ radiation source mounted on a WissEl Mössbauer driving unit operating in constant acceleration mode. To record spectra at low temperatures (4.3 K) and high applied magnetic fields (5 T), a liquid helium bath cryostat was employed. Using a superconducting magnet in split-pair geometry, a homogeneous magnetic field could be applied at the sample position, with the field being parallel to the γ-ray propagation direction.

Operando X-ray absorption spectroscopy (XAS) measurements. XAS measurements were conducted at the PETRA II P64 Advanced EXAFS beamline at DESY at the Co (7708.9 eV) and Fe (7112.0 eV) K-edge. Samples were measured dry in as-prepared state, *operando* during OER at 1.8 V_{RHE} after a conditioning with 20 cyclic voltammograms from 1–1.8 V_{RHE} with 50 mV s^{-1} scan-rate and at 1.0 V_{RHE} after OER. Further details are given in ESI.†

Electrochemical characterization. Electrochemical measurements were performed in a conventional three-electrode cell using an Autolab potentiostat/galvanostat (PGSTAT12, Eco Chemie, Utrecht, The Netherlands) coupled to a Metrohm RDE rotator. A disc shaped glassy carbon electrode of geometric area 0.196 cm^2 modified with the catalysts was used as working electrode, Ag/AgCl/3 M KCl as the reference electrode and a platinum sheet as counter electrode. The measured potentials were converted to the reversible hydrogen electrode (RHE) scale using the following equation E *vs.* RHE = E *vs.* Ag/AgCl + 0.207 V + 0.059 V × pH. The pH value (14 for 1 M KOH) was determined using a pH meter. Prior to the experiments, the glassy carbon electrode was polished on a polishing cloth using different alumina pastes (3.0–0.05 μm) to obtain a mirror-like surface, followed by ultrasonic cleaning in water. For electrochemical measurements, the catalyst ink was prepared by dispersing 5.0 mg of the catalyst in a mixture of 990 μL ethanol and water (1 : 1) and 10 μL of a 5 wt% Nafion 117 solution by ultrasonication for 30 min. 3.92 μL of the catalyst suspension was drop-coated onto the polished glassy carbon electrode and dried in air at room temperature resulting in a mass loading of 0.10 mg cm^{-2}. Prior to the OER measurements, modified electrodes were subjected to continuous potential cycling in the potential window of 1 V to 2 V *vs.* RHE with a scan rate of 100 mV s^{-1} until reproducible voltammograms were obtained and LSV measurements for OER activity were recorded with a scan rate of 5 mV s^{-1} in a potential window of 1 V to 2 V *vs.* RHE. Electrochemical impedance spectroscopy (EIS) was performed at frequencies between 100 kHz and 0.1 Hz with an overpotential of 550 mV. The resistance of the solution was determined from the resulting Nyquist plot, and then later used for ohmic drop correction according to the relation, $E_c = E_m - iR$, where E_c is the corrected potential and E_m is the applied potential. All reported current densities were calculated using the geometric surface area of the electrode.

Author contributions

S. Saddeler and G. Bendt performed the synthesis and characterization (XRD, EDX, IR, Raman, CV) of the nanoparticles. Analysis of magnetic properties and Mössbauer spectroscopy measurements were performed by S. Salamon and J. Landers. *Operando* X-ray absorption spectroscopy (XAS) measurements were performed by F. T. Haase, J. Timoshenko, C. Rettenmaier, H. S. Jeon and A. Bergmann. The work was supervised by B. Roldan Cuenya, H. Wende and S. Schulz. The manuscript was written by all authors.

Conflicts of interest

There are no conflicts to declare.

Acknowledgements

This research was funded by the Deutsche Forschungsgemeinschaft (DFG; German Research Foundation) under Project 388390466 with the collaborative research center/transregio TRR 247 "Heterogeneous Oxidation Catalysis in the Liquid Phase"; subprojects B2 (HW), A4 (BRC) and C3 (StS). We are also thankful to Dr Heidelmann (DFG core facility ICAN, University of Duisburg-Essen) for TEM characterization. We acknowledge DESY (Hamburg, Germany), a member of the Helmholtz Association HGF, for the provision of experimental facilities. Parts of this research were carried out at PETRA III and we would like to thank Dr Vadim Murzin and Dr Wolfgang Caliebe for using the P64 beamline.

Notes and references

1 S. Trasatti, *J. Electroanal. Chem.*, 1999, **476**, 90.
2 X. Xu, Z. Zhong, X. Yan, L. Kang and J. Yao, *J. Mater. Chem. A*, 2018, **6**, 5999.
3 F. Yang, K. Sliozberg, I. Sinev, H. Antoni, A. Bähr, K. Ollegott, W. Xia, J. Masa, W. Grünert, B. Roldan Cuenya, W. Schuhmann and M. Muhler, *ChemSusChem*, 2017, **10**, 156.
4 Y. R. Hong, S. Mhin, K. M. Kim, W. S. Han, H. Choi, G. Ali, K. Y. Chung, H. J. Lee, S. I. Moon, S. Dutta, S. Sun, Y.-G. Jung, T. Song and H. Han, *J. Mater. Chem. A*, 2019, **7**, 3592.
5 P. Mei, Y. Yamauchi, M. Pramanik, A. Fatehmulla, A. M. Adhafiri, W. A. Farooq, Y. Bando, M. J. A. Shiddiky, Y. V. Kaneti, J. Lin and Y. Kim, *Electrochem. Commun.*, 2019, **104**, 106476.
6 J. Masa, S. Barwe, C. Andronescu, I. Sinev, A. Ruff, J. Kolleboyina, K. Elumeeva, B. Konkena, B. Roldan Cuenya and W. Schuhmann, *ACS Energy Lett.*, 2016, **1**, 1192.
7 Y. Shao, X. Xiao, Y. P. Zhu and T. Y. Ma, *Angew. Chem., Int. Ed.*, 2019, **58**, 14599.
8 J. Masa, I. Sinev, H. Mistry, E. Ventosa, M. de la Mata, J. Arbiol, M. Muhler, B. Roldan Cuenya and W. Schuhmann, *Adv. Energy Mater.*, 2017, **7**, 1700381.
9 J. Masa, C. Andronescu, H. Antoni, S. Seisel, K. Elumeeva, S. Barwe, S. Marti-Sanchez, J. Arbiol, I. Sinev, B. Roldan Cuenya, M. Muhler and W. Schuhmann, *ChemElectroChem*, 2019, **6**, 235.
10 L. Xu, Q. Jiang, Z. Xiao, X. Li, J. Huo, S. Wang and L. Dai, *Angew. Chem., Int. Ed.*, 2016, **55**, 5277.
11 X. Zhou, X. Shen, Z. Xia, Z. Zhang, J. Li, Y. Ma and Y. Qu, *ACS Appl. Mater. Interfaces*, 2015, **7**, 20322.
12 R. Li, D. Zhou, J. Luo, W. Xu, J. Li, S. Li, P. Cheng and D. Yuan, *J. Power Sources*, 2017, **341**, 250.
13 C.-F. Li, J.-W. Zhao, L.-J. Xie, J.-Q. Wu, Q. Ren, Y. Wang and G.-R. Li, *Angew. Chem., Int. Ed.*, 2021, **60**, 18129.
14 J.-W. Zhao, C.-F. Li, Z.-X. Shi, J.-L. Guan and G.-R. Li, *Research*, 2020, 6961578.
15 H. Xu, Z.-X. Shi, Y.-X. Tong and G.-R. Li, *Adv. Mater.*, 2018, **30**, 1705442.
16 S.-H. Ye, Z.-X. Shi, J.-X. Feng, Y.-X. Tong and G.-R. Li, *Angew. Chem., Int. Ed.*, 2018, **57**, 2672.
17 S. Han, S. Liu, S. Yin, L. Chen and Z. He, *Electrochim. Acta*, 2016, **210**, 942.
18 A. El Arrassi, Z. Liu, M. V. Evers, N. Blanc, G. Bendt, S. Saddeler, D. Tetzlaff, D. Pohl, C. Damm, S. Schulz and K. Tschulik, *J. Am. Chem. Soc.*, 2019, **141**, 9197.
19 T. Quast, H. B. Aiyappa, S. Saddeler, P. Wilde, Y.-T. Chen, S. Schulz and W. Schuhmann, *Angew. Chem., Int. Ed.*, 2021, **60**, 3576.
20 J. Huo and M. Wei, *Mater. Lett.*, 2009, **63**, 1183.
21 K. F. Ortega, S. Anke, S. Salamon, F. Özcan, J. Heese, C. Andronescu, J. Landers, H. Wende, W. Schuhmann, M. Muhler, T. Lunkenbein and M. Behrens, *Chem.–Eur. J.*, 2017, **23**, 12443.
22 A. Hajalilou, S. A. Mazlan, M. Abbasi and H. Lavvafi, *RSC Adv.*, 2016, **6**, 89510.
23 P. C. R. Varma, R. S. Manna, D. Banerjee, M. R. Varma, K. G. Suresh and A. K. Nigam, *J. Alloys Compd.*, 2008, **453**, 298.
24 V. Georgiadou, C. Kokotidou, B. Le Droumaguet, B. Carbonnier, T. Choli-Papadopoulou and C. Dendrinou-Samara, *Dalton Trans.*, 2014, **43**, 6377.
25 Y. Eom, M. Abbas, H. Noh and C. Kim, *RSC Adv.*, 2016, **6**, 15861.
26 N. V. Long, Y. Yang, T. Teranishi, C. M. Thi, Y. Cao and M. Nogami, *RSC Adv.*, 2015, **5**, 56560.
27 C. An, Y. Wang, Y. Huang, Y. Xu, C. Xu, L. Jiao and H. Yuan, *CrystEngComm*, 2014, **16**, 385.
28 S. Sun and H. Zeng, *J. Am. Chem. Soc.*, 2002, **124**, 8204–8205.
29 K. M. Nam, J. H. Shim, D. W. Han, H. S. Kwon, Y. M. Kang, Y. Li, H. Song, W. S. Seo and J. T. Park, *Chem. Mater.*, 2010, **22**, 4446.
30 R. Bussamara, W. W. M. Melo, J. D. Scholten, P. Migowski, G. Marin, M. J. M. Zapata, G. Machado, S. R. Teixeira, M. A. Novak and J. Dupont, *Dalton Trans.*, 2013, **42**, 14473.
31 S. Sun, H. Zeng, D. B. Robinson, S. Raoux, P. M. Rice, S. X. Wang and G. Li, *J. Am. Chem. Soc.*, 2004, **126**, 273.
32 K. M. Nam, J. H. Shim, D. W. Han, H. S. Kwon, Y. M. Kang, Y. Li, H. Song, W. S. Seo and J. T. Park, *Chem. Mater.*, 2010, **22**, 4446.

33 K. Parekh, R. V. Upadhyay, L. Belova and K. V. Rao, *Nanotechnology*, 2006, **17**, 5970.
34 L. Ajroudi, N. Mliki, L. Bessais, V. Madigou, S. Villain and C. Leroux, *Mater. Res. Bull.*, 2014, **59**, 49.
35 L. Kampermann, J. Klein, J. Korte, O. Kowollik, O. Pfingsten, T. Smola, S. Saddeler, T. H. Piotrowiak, S. Salamon, J. Landers, H. Wende, A. Ludwig, S. Schulz and G. Bacher, *J. Phys. Chem. C*, 2021, **125**, 14356.
36 K. Chakrapani, G. Bendt, H. Hajiyani, I. Schwarzrock, T. Lunkenbein, S. Salamon, J. Landers, H. Wende, R. Schlögl, R. Pentcheva, M. Behrens and S. Schulz, *ChemCatChem*, 2017, **9**, 2988.
37 K. Chakrapani, G. Bendt, H. Hajiyani, T. Lunkenbein, M. T. Greiner, L. Masliuk, S. Salamon, J. Landers, R. Schlögl, H. Wende, R. Pentcheva, S. Schulz and M. Behrens, *ACS Catal.*, 2018, **8**, 1259.
38 Q. Song and Z. J. Zhang, *J. Am. Chem. Soc.*, 2004, **126**, 6164.
39 K. M. Nam, J. H. Shim, D. W. Han, H. S. Kwon, Y. M. Kang, Y. Li, H. Song, W. S. Seo and J. T. Park, *Chem. Mater.*, 2010, **22**, 4446.
40 L. T. Lu, N. T. Dung, L. D. Tung, C. T. Thanh, O. K. Quy, N. V. Chuc, S. Maenosono and N. T. K. Thanh, *Nanoscale*, 2015, **7**, 19596.
41 Y. Eom, M. Abbas, H. Y. Noh and C. G. Kim, *RSC Adv.*, 2016, **6**, 15861.
42 Y. Kumar, A. Sharma and P. M. Shirage, *RSC Adv.*, 2017, **7**, 55778.
43 Y. Kumar, A. Sharma, M. A. Ahmed, S. S. Mali, C. K. Hong and P. M. Shirage, *New J. Chem.*, 2018, **42**, 15793.
44 M. Hennous, E. V. Ramana, D. M. Tobaldi, B. F. O. Costa, M. A. Valente, J. Labrincha and M. Karmaoui, *New J. Chem.*, 2019, **43**, 10259.
45 S. Saddeler, U. Hagemann and S. Schulz, *Inorg. Chem.*, 2020, **59**, 10013.
46 I.-H. Jung, S. A. Decterov, A. D. Pelton, H.-M. Kim and Y.-B. Kang, *Acta Mater.*, 2004, **5**, 507.
47 H. Jalili, B. Aslibeiki, A. Ghotbi Varzaneh and V. A. Chernenko, *Beilstein J. Nanotechnol.*, 2019, **10**, 1348.
48 S. Mozaffari, W. Li, C. Thompson, S. Ivanov, S. Seifert, B. Lee, L. Kovarik and A. M. Karim, *Nanoscale*, 2017, **9**, 13772–13785.
49 L. Lukashuk, N. Yigit, H. Li, J. Bernardi, K. Fottinger and G. Rupprechter, *Catal. Today*, 2019, **336**, 139.
50 Y. G. Borod'ko, S. I. Vetchinkin, S. L. Zimont, I. N. Ivleva and Y. M. Shul'ga, *Chem. Phys. Lett.*, 1976, **42**, 264.
51 R. Ji, C. Cao, Z. Chen, H. Zhai and J. Bai, *J. Mater. Chem. C*, 2014, **2**, 5944.
52 W. Zhang, X. Li, R. Zou, H. Wu, H. Shi, S. Yu and Y. Liu, *Sci. Rep.*, 2015, **5**, 11129.
53 L. Ouyang, L. Zhu, J. Jiang and H. Tang, *Anal. Chim. Acta*, 2014, **816**, 41.
54 B. Rivas-Murias and V. Salgueiriño, *J. Raman Spectrosc.*, 2017, **48**, 837.
55 M. A. Laguna-Bercero, M. L. Sanjuán and R. I. Merino, *J. Phys.: Condens. Matter*, 2007, **19**, 186217.
56 N. Bahlawane, P. H. T. Ngamou, V. Vannier, T. Kottke, J. Heberle and K. Kohse-Höinghaus, *Phys. Chem. Chem. Phys.*, 2009, **11**, 9224.
57 A. V. Raut, R. S. Barkule, D. R. Shengule and K. M. Jadhav, *J. Magn. Magn. Mater.*, 2014, **358–359**, 87.
58 Y. Hao, X. Wang and L. Li, *Nanoscale*, 2014, **6**, 7940.
59 A. Kasprzak, M. Popławska, M. Bystrzejewski, O. Łabędź and I. P. Grudziński, *RSC Adv.*, 2015, **5**, 85556.
60 G. Concas, G. Spano, C. Cannas, A. Musinu, D. Peddis and G. Piccaluga, *J. Magn. Magn. Mater.*, 2009, **321**, 1893.
61 N. Fontaíña-Troitiño, S. Liébana-Viñas, B. Rodríguez-González, Z.-A. Li, M. Spasova, M. Farle and V. Salgueiriño, *Nano Lett.*, 2014, **14**, 640.
62 C. C. L. McCrory, S. Jung, J. C. Peters and T. F. Jaramillo, *J. Am. Chem. Soc.*, 2013, **135**, 16977.
63 M. S. Ahmed, B. Choi and Y.-B. Kim, *Sci. Rep.*, 2018, **8**, 2543.
64 H. N. Nong, L. J. Falling, A. Bergmann, M. Klingenhof, H. P. Tran, C. Spöri, J. Timoshenko, G. Zichittella, A. Knop-Gericke, S. Piccinin, J. Pérez-Ramírez, B. Roldan Cuenya, R. Schlögl, P. Strasser, D. Teschner and T. E. Jones, *Nature*, 2020, **587**, 408.
65 A. Bergmann, T. E. Jones, E. Martinez Moreno, D. Teschner, P. Chernev, M. Gliech, T. Reier, H. Dau and P. Strasser, *Nat. Catal.*, 2018, **1**, 711.
66 E. A. Schultz-Sikma, H. M. Joshi, Q. Ma, K. W. Macrenaris, A. L. Eckermann, V. P. Dravid and T. J. Meade, *Chem. Mater.*, 2011, **23**, 2657.
67 J. Fester, M. Garcia-Melchor, A. S. Walton, M. Bajdich, Z. Li, L. Lammich, A. Vojvodic and J. V. Lauritsen, *Nat. Commun.*, 2017, **8**, 14169.
68 J. Kim, W. H. Doh, Y. Kim, K.-J. Kim and J. Y. Park, *ACS Appl. Energy Mater.*, 2019, **2**, 8580.
69 P. F. Liu, S. Yang, L. R. Zheng, B. Zhang and H. G. Yang, *J. Mater. Chem. A*, 2016, **4**, 9578.
70 J. Dittmer, L. Iuzzolino, W. Dörner, H.-F. Nolting, W. Meyer-Klaucke and H. Dau, *Photosynthesis: Mechanisms and Effects*, 1998, p. 1339.
71 H. Dau, P. Liebisch and M. Haumann, *Anal. Bioanal. Chem.*, 2003, **376**, 562.
72 M. Risch, K. Klingan, F. Ringleb, P. Chernev, I. Zaharieva, A. Fischer and H. Dau, *ChemSusChem*, 2012, **5**, 542.
73 A. Bergmann, E. Martinez-Moreno, D. Teschner, P. Chernev, M. Gliech, J. F. de Araújo, T. Reier, H. Dau and P. Strasser, *Nat. Commun.*, 2015, **6**, 8625.
74 T. Wu, S. Sun, J. Song, S. Xi, Y. Du, B. Chen, W. A. Sasangka, H. Liao, C. L. Gan, G. G. Scherer, L. Zeng, H. Wang, H. Li, A. Grimaud and Z. J. Xu, *Nat. Catal.*, 2019, **2**, 763.